



**QUEEN'S  
UNIVERSITY  
BELFAST**

## **Cement As a Waste Form for Nuclear Fission Products: The Case of $^{90}\text{Sr}$ and Its Daughters**

Dezerald, L., Kohanoff, J. J., Correa, A. A., Caro, A., Pellenq, R. J-M., Ulm, F. J., & Saúl, A. (2015). Cement As a Waste Form for Nuclear Fission Products: The Case of  $^{90}\text{Sr}$  and Its Daughters. *Environmental Science and Technology*, 49(22), 13676-13683. <https://doi.org/10.1021/acs.est.5b02609>

**Published in:**  
Environmental Science and Technology

**Document Version:**  
Peer reviewed version

**Queen's University Belfast - Research Portal:**  
[Link to publication record in Queen's University Belfast Research Portal](#)

### **Publisher rights**

© 2015 American Chemical Society

This document is the Accepted Manuscript version of a Published Work that appeared in final form in *Environmental Science and Technology*. © American Chemical Society after peer review and technical editing by the publisher. To access the final edited and published work see <http://pubs.acs.org/doi/10.1021/acs.est.5b02609>

### **General rights**

Copyright for the publications made accessible via the Queen's University Belfast Research Portal is retained by the author(s) and / or other copyright owners and it is a condition of accessing these publications that users recognise and abide by the legal requirements associated with these rights.

### **Take down policy**

The Research Portal is Queen's institutional repository that provides access to Queen's research output. Every effort has been made to ensure that content in the Research Portal does not infringe any person's rights, or applicable UK laws. If you discover content in the Research Portal that you believe breaches copyright or violates any law, please contact [openaccess@qub.ac.uk](mailto:openaccess@qub.ac.uk).

# Cement as a waste form for nuclear fission products: the case of $^{90}\text{Sr}$ and its daughters

Lucile Dezerald,<sup>1,2</sup> Jorge J. Kohanoff,<sup>3</sup> Alfredo A. Correa,<sup>4</sup> Alfredo Caro,<sup>5</sup> Roland J.-M. Pellenq,<sup>1,2,6</sup> Franz J. Ulm,<sup>1,2</sup> and Andrés Saúl\*<sup>1,2,6</sup>

<sup>1</sup>*Department of Civil and Environmental Engineering,  
Massachusetts Institute of Technology,*

<sup>2</sup>*MultiScale Material Science for Energy and Environment, UMI 3466 CNRS-MIT,  
77 Massachusetts Avenue, Cambridge CA 02139, USA*

<sup>3</sup>*Atomistic Simulation Centre, Queen's University Belfast,  
Belfast BT7 1NN, United Kingdom*

<sup>4</sup>*Condensed Matter and Materials Division,  
Physical and Life Sciences Directorate,  
Lawrence Livermore National Laboratory, Livermore, California 94550, USA*

<sup>5</sup>*Los Alamos National Laboratory, Los Alamos New Mexico 87545, USA*

<sup>6</sup>*Aix-Marseille University, CINaM-CNRS UMR 7325  
Campus de Luminy, 13288 Marseille cedex 9, France*

## Abstract

One of the main challenges faced by the nuclear industry is the long-term confinement of nuclear waste. Because it is inexpensive and easy to manufacture, cement is the material of choice to store large volumes of radioactive materials, in particular the low-level medium-lived fission products. It is therefore of utmost importance to assess the chemical and structural stability of cement containing radioactive species. Here, we use *ab-initio* calculations based on density functional theory (DFT) to study the effects of  $^{90}\text{Sr}$  insertion and decay in C-S-H (calcium-silicate-hydrate) in order to test the ability of cement to trap and hold this radioactive fission product and to investigate the consequences of its  $\beta$ -decay on the cement paste structure. We show that  $^{90}\text{Sr}$  is stable when it substitutes the  $\text{Ca}^{2+}$  ions in C-S-H, and so is its daughter nucleus  $^{90}\text{Y}$  after  $\beta$ -decay. Interestingly,  $^{90}\text{Zr}$ , daughter of  $^{90}\text{Y}$  and final product in the decay sequence, is found to be unstable compared to the bulk phase of the element at zero K but stable when compared to the solvated ion in water. Therefore cement appears as a suitable waste form for  $^{90}\text{Sr}$  storage.

Long-term confinement of radioelements produced by nuclear fission is one of the main challenges faced by the nuclear industry. The primary focus of the nuclear waste storage research has long been oriented towards host materials that can handle the large structural damage induced by the high-energy  $\alpha$ -decay of actinides.<sup>1,2</sup> However, the need for optimizing the vitrification process of actinides<sup>1</sup> and for increasing the capacity of repositories<sup>3</sup> has prompted the investigation of other forms of containers specifically targeted at low- and medium-level waste. Such containers became urgently needed after the Fukushima disaster, where large volumes of contaminated soils, water and buildings had to be quickly handled.<sup>4-7</sup> The main concern lies in the management of the medium-lived  $\beta^-$ -emitter fission products,  $^{137}\text{Cs}$  and  $^{90}\text{Sr}$ .<sup>4,5</sup> These represent the largest **fraction of the nuclear waste by activity**,<sup>8</sup> and have been found in the surrounding areas and in the cooling water of the damaged power plants.<sup>4,5</sup> They present important health risks:  $^{137}\text{Cs}$   $\beta^-$  decay is followed by a hazardous  $\gamma$  emission, while  $^{90}\text{Sr}$  can contaminate the animal and human population due to its ability to replace the isovalent Ca ions that constitute bones and teeth (hence the name *bone seeker*). This is particularly dangerous as  $\beta$ -emission in the bone produces a low-energy electron cascade that can reach stem cells in the bone marrow, this being a major cause of leukaemia.

$\beta^-$  decay produces modifications of the host matrix chemistry and can also influence its mechanical properties. The three main processes following  $\beta$ -decay are: (1) the emission of the  $\beta$  electron at MeV energies, (2) the recoil of the transmuted nucleus with kinetic energies in the eV range due to conservation of momentum, and (3) the electronic rearrangement around the transmuted nucleus due to the sudden increase in nuclear charge ( $Z \rightarrow Z + 1$ ). All of these processes interact with the host in different ways.<sup>1,9-11</sup> Recent theoretical studies of the effects of transmutation due to  $\beta^-$  decay of  $^{137}\text{Cs}$  and  $^{90}\text{Sr}$  in ceramics and oxides<sup>12</sup> showed important chemical and structural modifications of the host material in the case of radioparagenesis<sup>11,13</sup> in which a solid-state daughter phase is derived radiogenically by a parent phase. These studies enable the design of waste forms with improved mechanical properties by means of transmutation, thus opening a promising avenue for long-term nuclear waste containment. A different, although related matter is the assessment of the aging of materials partially contaminated by hosting nuclear waste, which is the main focus of the

present work.

Here we investigate the local effects of  $^{90}\text{Sr}$  contamination and transmutation on cement.  $^{90}\text{Sr}$  (half-life 28.79 years) undergoes two successive  $\beta^-$  decays to  $^{90}\text{Y}$  (half-life 64 hours), and to  $^{90}\text{Zr}$  (stable). Compared to specifically designed glass or ceramic nuclear waste containers, cement is inexpensive, easy to manufacture, easy to formulate by mixing with other materials such as blast furnace slag,<sup>14</sup> and it benefits from centuries of use and decades of research related to the civil engineering industry. This makes cement the primary candidate for large volumes of low-level nuclear waste storage in post-accidental conditions. So far, most of the research on irradiated cement has focused on its ability to capture radioelements, and on their leaching from cement containers.<sup>8,15–21</sup> As mentioned above,  $^{90}\text{Sr}$  capture in cement is very likely because of Ca-Sr isovalence, Ca being present in C-S-H (calcium-silicate-hydrate), which is the principal binding product of cement hydration.<sup>22–24</sup> Although recent atomistic simulations showed that  $^{90}\text{Sr}$  capture by C-S-H does not modify the elastic properties of cement,<sup>25</sup> the consequences of  $^{90}\text{Sr}$  transmutation via  $\beta^-$  decay on C-S-H structure and chemical properties are still largely unknown.

In this work we investigate the consequences of  $^{90}\text{Sr}$  transmutation in C-S-H using calculations based on Density Functional Theory (DFT), which is an appropriate tool to account for the electronic and chemical properties of the cement paste as well as those of the investigated radionuclides. The chemical and physical mechanisms at stake in  $^{90}\text{Sr}$  capture were investigated by substituting **Ca atoms** in the atomistic model of C-S-H proposed in References [26–28].  $^{90}\text{Sr}$  was then successively replaced by its daughter nucleus,  $^{90}\text{Y}$  and  $^{90}\text{Zr}$ , to study the stability of these elements in cement paste. DFT molecular dynamics (DFMD) simulations were then performed to investigate the possible chemical and structural modifications induced locally in C-S-H contaminated by  $^{90}\text{Sr}$  and its successive transmutations.

## METHODOLOGY

C-S-H, the principal binding phase responsible of the strength of cementitious materials, precipitates as nanoscale clusters when mixing water with di-calcium ( $\text{C}_2\text{S}$ ) and tri-calcium silicate ( $\text{C}_3\text{S}$ ). Given its complex structure and composition, the atomic structure of C-S-H has traditionally been based on Taylor’s postulate that C-S-H is a structurally imperfect layered hybrid of two natural minerals,<sup>29</sup> tobermorite of 14 Å interlayer spacing<sup>30</sup> and

jennite.<sup>31</sup> These minerals reproduce the laminar structure of C-S-H where calcium ions are located between layers of silicate chains. An overview of the tobermorite and jennite-based C-S-H models used in the literature is given in Refs. [32 and 33]. However, limitations of these models emerged when it became possible to further characterize experimentally the C-S-H molecular composition, notably the average calcium to silicon ratio ( $C/S = 1.7$ ) and the density of the C-S-H particle ( $2.6 \text{ g/cm}^3$ ).<sup>34-37</sup> These values cannot be obtained from either tobermorite  $14 \text{ \AA}$  ( $C/S = 0.83$  and  $2.18 \text{ g/cm}^3$ ) or jennite ( $C/S = 1.5$  and  $2.27 \text{ g/cm}^3$ ). A solid solution model proposed recently<sup>38</sup> corrects most of these problems.

The atomic structure for C-S-H used in this work has recently been proposed in order to bridge the gap between atomic-scale simulations and experiments.<sup>26-28</sup> It is presented in Fig. 1 and was generated following the procedure reported in Ref. [26].

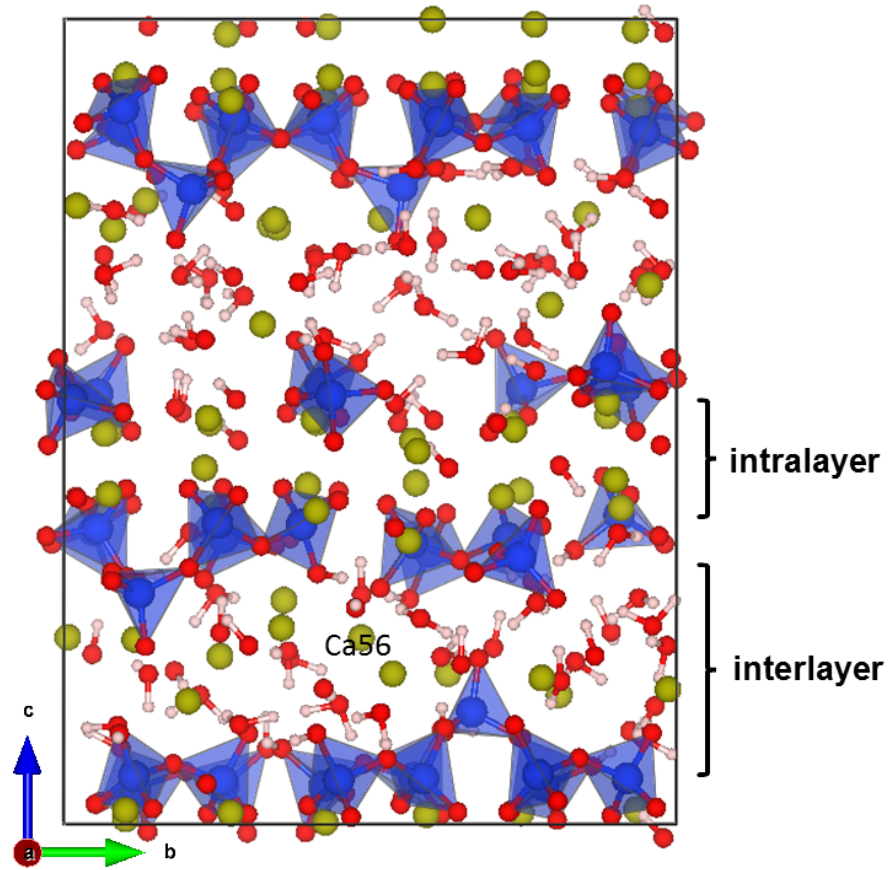


Figure 1. (color online) Schematic representation of the C-S-H structure. Hydrogen atoms are in white, oxygen atoms in red, calcium in yellow, and Si in blue. The corner sharing  $\text{SiO}_4^{4-}$  tetrahedra forming the silicate chains are also shown.

This model was shown to reproduce accurately both the structural and chemical properties of C-S-H. Among other properties, water content, silica chain lengths, and pair distribution functions were compared satisfactorily to small angle neutron scattering (SANS), solid-state nuclear magnetic resonance (NMR) and x-ray diffraction (XRD) experiments, respectively. The cell contains 501 atoms and has the chemical composition  $\text{Ca}_{72}\text{Si}_{44}\text{O}_{235}\text{H}_{150}$ , with a C/S ratio of 1.64 and a density of  $2.33 \text{ g/cm}^3$  in very good agreement with experimental data.<sup>34–37</sup> Figure 1 shows the silicate chains formed by corner sharing  $\text{SiO}_4^{4-}$  tetrahedra. These chains, which form the characteristic layered structure of C-S-H, have been randomly broken to obtain the desired C/S ratio.<sup>26–28</sup> It can also be seen that the  $\text{Ca}^{2+}$  ions appear in two distinct environments: intralayer and interlayer. Water, in the form of  $\text{H}_2\text{O}$  molecules and  $\text{OH}^-$  groups, is present in the interlayer space.

First-principles electronic structure calculations were performed within the DFT framework using the Quantum-espresso plane-wave code.<sup>39</sup> We used the Perdew-Burke-Ernzerhof generalized gradient approximation (PBE-GGA)<sup>40</sup> and ultrasoft pseudopotentials with explicit semi-core electrons. The plane-wave cutoff for the Kohn-Sham orbitals was set to 80 Ry and all the calculations were performed at constant volume with a single  $\mathbf{k}$ -point (the  $\Gamma$ -point). Residual forces on the atoms after geometric relaxation were smaller than  $10^{-3} \text{ Ry}/a_0$ .

We first performed a 1.2 ps DFMD simulation at 300 K to check the local stability of the C-S-H structure used. We then performed a set of DFMD simulations to study possible displacements of the substitute radioelements in the cement matrix.

Given the computational load of DFMD calculations, the latter were performed for only one of the 72 Ca sites (site number 56, interlayer, indicated in Fig. 1). These simulations were aimed at verifying that the preferred site for the substituting atoms corresponded to the site previously occupied by the Ca ion. When this was not the case, the simulations allowed us to investigate the structural modifications induced by  $^{90}\text{Sr}$  insertion and decay in C-S-H.

## RESULTS

**Substitution and decay of  $^{90}\text{Sr}$  in Ca sites.** C-S-H contamination was investigated by substituting one by one each Ca **atom** by Sr. The chemical effects of  $^{90}\text{Sr}$  transmutation

via  $\beta^-$  decay in C-S-H were then studied by substituting Ca with Y and Zr, successively. The C-S-H cell after substitution, denoted  $\text{Ca}_{n-1}\text{X}$  where X stands for Sr, Y or Zr, has the chemical composition  $\text{Ca}_{71}\text{XSi}_{44}\text{O}_{235}\text{H}_{150}$ . Each substitution is followed by relaxation of the atomic positions. The substitution energy  $\Delta E_{\text{X}}(i)$  **calculated with respect to the bulk phases of the elements at 0 K** is defined as:

$$\Delta E_{\text{X}}(i) = E_{\text{Ca}_{n-1}\text{X}}(i) - E_{\text{Ca}_n} + E_{\text{Ca}}^{\text{bulk}} - E_{\text{X}}^{\text{bulk}} \quad (1)$$

where  $E_{\text{Ca}_{n-1}\text{X}}(i)$  is the energy of the cell containing element X at site  $i$ ,  $E_{\text{Ca}_n}$  is the energy of C-S-H before substitution, and  $E_{\text{X}}^{\text{bulk}}$  are the energies of the bulk phases: face-centered cubic for Ca and Sr, and hexagonal close-packed for Y and Zr. The calculated substitution energies for Sr, Y and Zr in each one of the 72 Ca sites of the simulation cell are presented in Fig. 2.

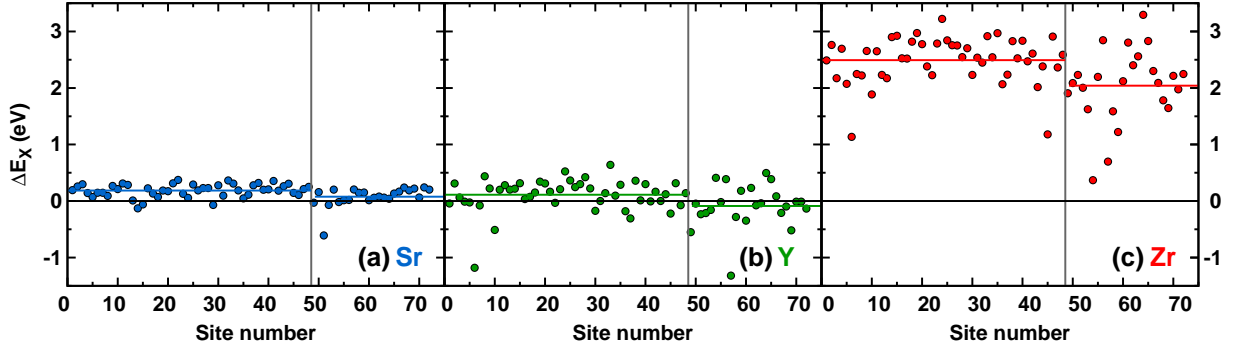


Figure 2. (color online) Substitution energies for (a) Sr, (b) Y, and (c) Zr (circles) in the 72 Ca sites **calculated with respect to the bulk phases at 0K**. The vertical lines separate the first 48 sites corresponding to intralayer sites trapped between silicate chains and the remaining 24 sites (number 49 to 72) corresponding to the interlayer area. The horizontal lines stand for the average substitution energy value, calculated separately for the intralayer and interlayer.

Figure 2(a) shows the results for Sr. As expected from the isovalence between Sr and Ca, the substitution energy is generally low (0.15 eV on average), with 7 negative values. Negative  $\Delta E_{\text{Sr}}$  values indicate sites where Sr is more stable than Ca, and will tend to substitute it, thus contaminating the sample. To further analyze the data, we divided Fig. 2(a) into two sections marked by a vertical line: the first 48 sites correspond to intralayer Ca sites trapped between silicate chains and the remaining 24 sites (number 49 to 72)

correspond to the interlayer area, where the Ca ions co-exists with water molecules and  $\text{OH}^-$  groups. We also show in Fig. 2(a) the average substitution energy calculated separately for the intra and interlayer with a horizontal blue line; the substitution energies for  $^{90}\text{Sr}$  are, on average, lower in the interlayer (0.08 eV) than in the intralayer (0.19 eV).

It is interesting to note here that due to the configurational entropy contribution to the free energy, solution energies of this order of **magnitude** imply quite a large solubility limit even at room temperature. A regular solution model with a solution energy of 0.08 eV gives, for example, a solubility at room temperature of 4%, thus providing an order of magnitude of the amount of Sr that can be incorporated into cement.

These results are in good agreement with experimental observations showing that Sr uptake in cement occurs preferably by Ca substitution in C-S-H.<sup>22,23</sup> They also showed that the  $\text{Sr}^{2+}$ - $\text{Ca}^{2+}$  exchange might occur in the interlayers of the C-S-H phases.<sup>23</sup> The presence of other isotopes of Sr arising from the raw materials ( $^{86}\text{Sr}$  and  $^{87}\text{Sr}$ ) in standard cement should not modify this mechanism since the quantity is negligible (approximately 0.1%).

Table 1. Average substitution energy  $\Delta E_{\text{X}}$  **calculated relative to the bulk phases at 0K (columns 2 to 4) and to the hydrated forms of the ions (columns 5 to 7) (eV)** on all the 72 substitution Ca sites and separately on the 48 intralayer sites and on the 24 interlayer sites.

|    | Relative to the bulk phase at 0 K |            |            | Relative to the hydrated forms of the ions |            |            |
|----|-----------------------------------|------------|------------|--|------------|------------|
|    | Total                             | Intralayer | Interlayer | Total                                      | Intralayer | Interlayer |
| Sr | 0.15                              | 0.19       | 0.08       | 0.23                                       | 0.27       | 0.16       |
| Y  | 0.05                              | 0.11       | -0.09      | -3.32                                      | -3.26      | -3.46      |
| Zr | 2.34                              | 2.49       | 2.04       | -6.43                                      | -6.28      | -6.73      |

In order to investigate the chemical effects of  $^{90}\text{Sr}$   $\beta^-$  decay on C-S-H structure, we calculated the substitution energy of Y **relative to the bulk phases at 0 K** in all 72 Ca site. The results are presented in Fig. 2(b) and the calculated average substitution energies are gathered in Table 1. Fig. 2(b) shows that the substitution energy of Y is generally lower than that of Sr, with a larger dispersion and an average value of 0.05 eV. Overall, 28 sites substituted with Y display a negative  $\Delta E_{\text{Y}}$ . Y is consequently more stable in C-S-H than Sr, which could seem surprising because, with a theoretical charge of 3+, Y is not isovalent with Ca. Nevertheless, it has been shown experimentally that other 3+ charged metals (Nd,



Cm and Eu) can be accommodated by substitution of Ca in C-S-H.<sup>41–44</sup> For Y, the average substitution energy is lower but still positive in the intralayer region (0.11 eV), and it is now negative in the interlayer spacing (-0.09 eV). We also notice that the difference between the average substitution energy in the intra and interlayer regions is larger for <sup>90</sup>Y (0.20 eV) than for <sup>90</sup>Sr (0.11 eV).

The substitution energies of <sup>90</sup>Zr, daughter nucleus of <sup>90</sup>Y also through  $\beta^-$  decay, **using the same bulk references**, are given for the 72 sites in Fig. 2(c) and Table 1. Contrary to Sr and Y, the calculated energies are all positive, large and widely dispersed around the average value of 2.34 eV, which is more than one order of magnitude larger than that of Sr. Fig. 2(c) shows again an enhanced stability upon substitution in the interlayer relative to the intralayer region, while the energy difference between intra and interlayer substitution is the largest (0.45 eV).

The substitution energies that we presented here use the energies of the bulk phases at 0 K as a reference. Another possibility would be to use the solvation energy of the corresponding hydrated forms of the ions. To convert from the elemental forms to the hydrated ones, one should add **to the bulk energies  $E_X^{\text{bulk}}$  in Eq. (1)** two positive quantities, the **corresponding** cohesion and ionization energies and a negative one, the hydration energy of the **corresponding** ions. Using the values reported in Ref. [45] for the latter, we have found that the new reference shifts the points in Figures 2(a), 2(b), and 2(c) by 0.08, -3.37, and -8.77 eV respectively. With respect to the hydrated ions, the average substitution energies become 0.23, -3.23, and -6.43 eV **(see Table 1)**.

The most important difference is the highly negative value of the substitution energies for Zr originated by the unstable character of the hydrated forms of  $\text{Zr}^{4+}$  which has been reported to be stable only in dilute solutions with a pH below 0.<sup>46</sup>

**This is an important result meaning that substitution of Ca by Zr is unfavored when compared to the bulk phases at 0 K but the substitution is very likely when compared to the hydrated forms in water. However, in** order to state a definitive conclusion on the most suitable adsorption site for Zr a systematic study of all possible compounds and coordination complex has to be performed. Such study is beyond the scope of the present paper.

Finally, we have also verified that Sr in C-S-H prefers to substitute Ca rather than Si (present in the silicate chains). Substitution energies **with respect to the bulk phases**

obtained for Sr replacing Si are around 4 eV, which are 10 times larger than those obtained when Sr replaces Ca, thus rendering this process extremely unlikely. This is expected from the charge imbalance locally originated by such a substitution.

**Effects of temperature on contaminated C-S-H.** To further investigate the effect of  $^{90}\text{Sr}$  contamination and decay on the structure of C-S-H, we performed DFMD simulations at 300 K for 1.2 ps. The goal of this is to investigate if the presence of Sr and its daughter nuclei Y and Zr can lead to structural modifications of the cement paste, or if they are likely to stay in former Ca sites as assumed above. Given the computational cost of such calculations, we focused on a single Ca site, number 56 in our notation, which is situated in the interlayer spacing. This site is a good candidate to test our hypotheses. Since its substitution energy is average for Sr and larger than average for Y and Zr, the daughters are likely to migrate.

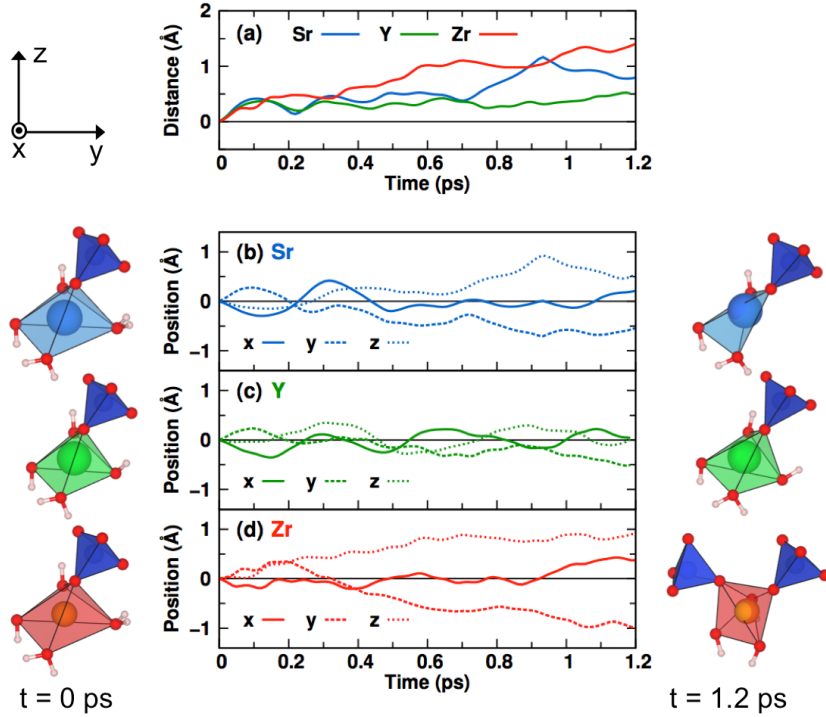
For the DFMD simulations, we have used a temperature control based on velocity rescaling. In this scheme, the velocities are rescaled if the average temperature and the target temperature of the system differ in more than a certain tolerance, which here was set to 50K.

The thermal relaxation of Sr56, Y56 and Zr56 during the simulated time range was investigated by studying the displacements of the three substitute atoms. The results are presented in Fig. 3. The displacements were found to be rather small, not exceeding 1.5 Å, as one would expect in such short simulations. Fig. 3(a) shows that Sr56 (in blue) travels a maximum distance of 0.5 Å before 0.6 ps, after which it starts moving away from its original position rather quickly before stabilizing again. Y56 does not move much away from its original position. The maximum total displacement calculated remains under 0.5 Å over the complete DFMD simulation. The displacement of Zr56 (orange) is qualitatively different from Sr56 and Y56. Not only it is larger, but it increases monotonically from the start of the simulation, thus suggesting that Zr is not stable in the interlayer Ca sites.

The distance traveled by Sr56, Y56, and Zr56 can be decomposed into the contributions along the  $x$ ,  $y$  and  $z$  directions, as shown in Fig. 3(b), (c), and (d). We also show in Fig. 3 the coordination polyhedra around Sr56, Y56, and Zr56 at  $t = 0$  ps (left) and 1.2 ps (right).

Figure 3(b) shows that the large increase of distance starting at 0.6 ps in Sr56 is mainly due to displacements of equal amplitudes in the  $y$  and  $z$  directions, i.e. along the  $[01\bar{1}]$  direction which is perpendicular to the silicate layers (see Fig. 1). The variations in the  $x$

direction are small after thermalization, and stabilize close to zero after 0.4 ps. The main difference in the coordination polyhedra is the elimination of one of the hydration waters.



251

Figure 3. (color online) (a) Distance traveled by Sr56 (blue), Y56 (green) and Zr56 (orange) as a function of time; and evolution of the position of (b) Sr56, (c) Y56, and (d) Zr56 with time at 300 K, along the  $x$  (plain lines),  $y$  (dashed lines), and  $z$  (dotted lines) direction. The corresponding coordination polyhedra formed by X56-O are shown at  $t = 0$  ps and  $t = 1.2$  ps respectively on the left and right of (b) to (d)).

The same is valid for Zr56 (see Fig. 3(d)), where the largest displacements are also along the  $[01\bar{1}]$  direction (see Fig. 3(d)), although in this case the displacement continues increasing over time. In consequence, the surroundings of Zr56 are modified during the simulation, the major difference being that **the coordination evolves from one  $\text{SiO}_4^{4-}$  tetrahedron, two hydration waters and two OH groups at  $t = 0$  ps to two  $\text{SiO}_4^{4-}$  tetrahedra and three OH groups at  $t = 1.2$  ps (see Fig. 3(d)).**

Figure 3(c) shows that the total displacement calculated for Y56 is due to small oscillations of this atom around its original position in the three directions, due to thermal motion,

and no important modification is visible on the Y56-O polyhedron. The similarity between the O-Ca and O-Y bond lengths (see below) is certainly at the origin of this result.

The configurations reached after 1.2 ps of DFMD simulation were relaxed back to 0 K using the same convergence criterion on the total energy and forces used for the substitution energy calculations. This calculation was performed in order to verify whether the ground state energies obtained after the thermal rearrangement are similar to those displayed in Fig. 2. Before the DFMD simulation, the Y-Sr energy difference was 0.37 eV and the Zr-Sr energy difference was 2.82 eV, i.e. site 56 did not exactly respect the global trend according to which Y is slightly more stable than Sr. After the 1.2 ps DFMD simulation and quenching back to 0 K, we found that the substitution energy for site 56 reverts, now conforming to the hierarchy previously calculated: it is lowest for Y, small for Sr and large for Zr. The energy differences are now -0.05 eV for Y-Sr and 2.88 for Zr-Sr, thus validating the previous approach.

## DISCUSSION

**Pair distribution.** In order to investigate the physical origin of the relative stability of Sr, Y, and Zr in the cement paste, we calculated the pair distribution function (PDF) for the X-O bonds at 0 K ( $X = \text{Ca, Sr, Y, Zr}$ ). We compare the PDF with the average bond lengths obtained by Shannon from an extensive compilation of crystallographic data.<sup>47,48</sup> The pair distributions are shown as solid black lines in Figures 4(a) to (d).

The PDF for Ca-O is shown in Fig. 4(a) along with the value of 2.40 Å tabulated by Shannon for the Ca-O bond length, which is indicated by a vertical line. The average Ca-O bond length was calculated to be 2.43 Å, in good agreement with the tabulated value. These values are reported in Table 2.

The Sr-O PDF is shown in Fig. 4(b). Its maximum is shifted to larger distances compared to the Ca-O pair distribution, in good agreement with the tabulated value. The corresponding Sr-O bond length, 2.56 Å, is also close to the tabulated value of 2.58 Å. The Y-O pair distribution shown in Fig. 4(c) is shifted towards shorter distances compared to the Ca-O pair distribution. The bond length was found to be 2.36 Å, which is slightly larger than the tabulated bond length of 2.30 Å. The 0 K Zr-O bond length is the shortest (2.23 Å) and displays the largest discrepancy with the tabulated value of 2.12 Å. This can be correlated

to the large substitution energies **with respect to the bulk phases** found for Zr in the previous section.

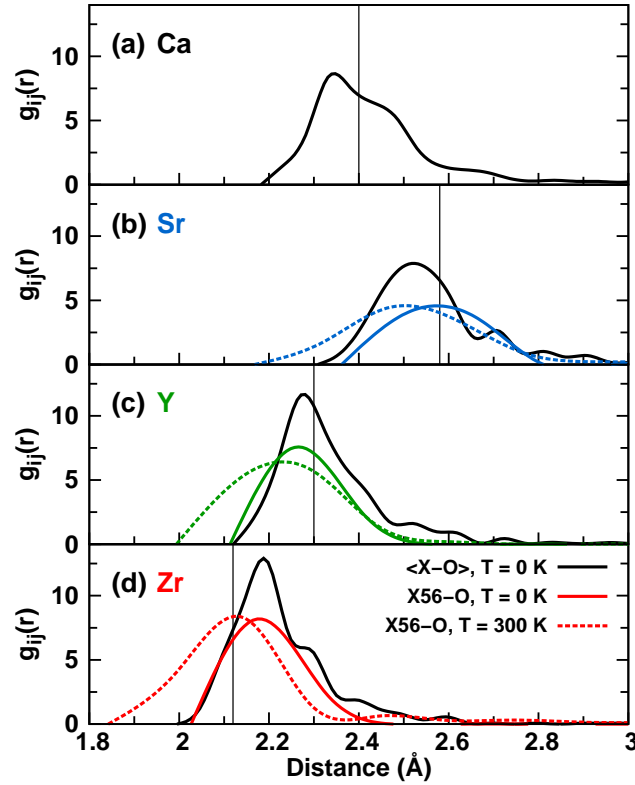


Figure 4. (color online) Pair distribution functions for the O- (a) Ca, (b) Sr, (c) Y, and (d) Zr bonds calculated on average for all sites at 0 K (black lines), for site 56 at 0 K (solid colored lines), and for site 56 at 300 K (colored dotted line). Cubic splines have been used to smooth the pair distribution functions.

The pair distributions for the intralayer and interlayer sites do not show substantial differences. To illustrate this point, we report in Table 2 the average bond length for these two regions. The maximum difference calculated between the intra and interlayer X-O distances is 0.02 Å for Zr, which is very small compared to differences among elements and hence does not explain the general preference for Ca substitution in the interlayer region. In Figures 4(b) to (d) the colored lines show the pair distributions calculated for the X56-O bond at two different temperatures: 0 K (solid colored lines) and 300 K, averaged over the stable 1 ps part of the DFMD simulation (dashed colored lines).

The pair distribution for Sr56-O at 0 K (Fig. 4 (b)) is close to the average Sr-O pair distribution resulting in bond lengths that are similar (see Table 2). The same applies to

the pair distributions and bond lengths calculated for site 56 replaced by Y and Zr at 0 K, thus confirming that site 56 is a good candidate to represent the average properties of these atoms in C-S-H.

Table 2. X-O bond lengths in the C-S-H structure. The first three columns report the average bond length calculated on all sites (Total) and separately in the intralayer (Intra) and in the interlayer (Inter) sites at 0 K. The next two columns give the X-O bond length calculated for atom X in site 56 at 0 K and at 300 K. The last column gives the values obtained from Table 1 of Ref. [48] (Shannon1976). For easy of comparison we consistently used the reported values for coordination number VI and the formal charges 2+, 2+, 3+, and 4+ for Ca, Sr, Y, and Zr respectively. We did not take into account the distortion of the coordination polyhedra or the bond length distribution. All the values are given in Å.

|    | Average, 0 K |       |       | Site 56 |       | Shannon1976 |
|----|--------------|-------|-------|---------|-------|-------------|
|    | Tot          | Intra | Inter | 0 K     | 300 K |             |
| Ca | 2.43         | 2.43  | 2.43  |         |       | 2.40        |
| Sr | 2.56         | 2.56  | 2.57  | 2.58    | 2.53  | 2.58        |
| Y  | 2.36         | 2.33  | 2.33  | 2.30    | 2.25  | 2.30        |
| Zr | 2.23         | 2.23  | 2.21  | 2.21    | 2.15  | 2.12        |

The stability of the contaminated C-S-H structure with temperature was investigated by calculating the pair distributions for the X56-O bonds on average at 300 K (dashed colored lines on Figures 4(b) to (d)), and comparing them to the pair distributions obtained at 0 K (solid colored lines). A general broadening of the PDF due to the temperature is visible on all three figures. A slight shift to shorter distances is also observed, which results in shorter average bond lengths (see Table 2). This result can be due to the ability of the mobile H<sub>2</sub>O molecules and OH<sup>-</sup> groups from the interlayer to rearrange and form shorter bonds with the substitutional atom under the effects of temperature.

Interestingly the average bond length of Zr56-O at 300K is very close to the tabulated value of 2.12 Å. In the beginning of the DFMD simulation, Zr56 is located in the interlayer spacing, surrounded by water molecules and OH<sup>-</sup> groups. Then, Zr56 migrates under the effects of temperature so that, after 0.5 ps, two of the seven nearest O atoms belong to silicate chains (SiO<sub>4</sub><sup>4-</sup> tetrahedron). Based on the latter observation and on the isovalency

of Zr with Si, it is natural to wonder whether or not it is convenient for Zr to substitute Si instead of Ca atoms in C-S-H. We investigated this possibility by substituting Zr for Si in seven (out of 44) sites. The calculated energies **with respect to the bulk phases** were all negative, varying from  $-2.15$  eV to  $-0.41$  eV, with an average value of  $-1$  eV. These energies are much lower than the ones reported in Figure 2(c), and indicate that Zr will certainly stabilize by interfering with the layered structure characteristic of C-S-H. Similar conclusions have been found for the uptake of other 4+ charged metals (Np, Th)<sup>24,49</sup> (Sn)<sup>50</sup> in C-S-H. More firm comparisons however require further investigation, e.g. via DFMD simulation over longer time scales using classical force fields to overcome the time-scale limitations imposed by the first-principles description of the interactions.

**Analysis of the charges.** In order to analyse the bonding characteristics we have calculated the Bader charges<sup>51</sup> for the configurations relaxed at 0 K using the Bader Charge Analysis tool.<sup>52</sup> In this method the atomic charge is defined as the nuclear charge minus the integral of the electronic density in a well-defined volume around the atom. The obtained charges are systematically smaller than the expected formal charges. The more ionic the bond the closer the Bader charge to the formal charge. In this way we obtained 72 values of the effective charge for Ca, Sr, Y and Zr. The average effective charges for all elements are reported in Table 3.

Table 3. Average effective charge calculated on all sites (Tot) and separately in the intralayer (Intra) and in the interlayer (Inter) sites. Charge of site X56 at 0 K and 300 K. The theoretical charge for each element is given for information in the first column. All charges are expressed in the elementary charge unit  $e$ .

|                  | Average         |       |       | Site 56 |
|------------------|-----------------|-------|-------|---------|
|                  | Tot             | Intra | Inter |         |
| Ca <sup>2+</sup> | $1.60 \pm 0.04$ | 1.59  | 1.61  | 1.60    |
| Sr <sup>2+</sup> | $1.62 \pm 0.04$ | 1.61  | 1.63  | 1.66    |
| Y <sup>3+</sup>  | $2.22 \pm 0.11$ | 2.21  | 2.23  | 2.22    |
| Zr <sup>4+</sup> | $2.28 \pm 0.41$ | 2.25  | 2.33  | 2.15    |

Ca and Sr are found to be isovalent, as expected, with an effective charge of approximately  $1.6e$  on average. This charge is close to the formal charge of these elements, which means

that the bonding of these systems is ionic, as expected. Y in Ca sites have an average charge of  $2.22e$ , which suggests that Y donates (on average) a large part of its valence electrons, exhibiting a charge state that is intermediate between the  $2+$  corresponding to the substituted atom, and its own ionic charge of  $3+$ , suggesting a more covalent bonding for this radioelement. This results in a slightly lower substitution energy for Y than that of Sr. Interestingly, Zr has an average charge of  $2.28e$ , similar to that of Y meaning significant covalency in this system. As the Zr charge in cubic  $\text{ZrO}_2$  is  $2.52e$ , the smaller average value of the charge means that despite the energy relaxation, the substitution sites originally optimized for  $\text{Ca}^{2+}$  do not have enough states available in the neighboring oxygen atoms to accept more electrons. This, combined with the pair distribution analysis, could explain the large substitution energies of Zr in Ca sites.

To understand the general preference for substitution in the interlayer we report in Table 3 the average effective charge calculated separately in the intra and interlayer regions. There is a small but systematic increase of the Bader charges in the interlayer sites with respect to the intralayer ones. This can be explained by the conspicuous presence of oxygen in the form of mobile  $\text{OH}^-$  groups in the interlayer. These can bind more easily to the substitutional ions, whereas in the intralayer the neighboring oxygens belong to the silicate chains and are thus less prone to accept electrons and stabilize the ions.

Finally, we note that the difference between inter and intralayer average effective charges increases along the radioactive decay sequence, from  $^{90}\text{Sr}$  to  $^{90}\text{Zr}$ . Indeed, the difference between the intralayer and interlayer average charge is the smallest for Sr and Y (around  $0.02e$ ) and four times larger for Zr ( $0.08e$ ). This result correlates with the substitution energy difference between the intralayer and the interlayer regions that also increases along the same decay sequence, as pointed out in the Results section. Similarly, the dispersion around the average value is the smallest in Sr, intermediate in Y and the largest in Zr, for both the substitution energies (see Fig. 2) and the Bader charges (see Table 3).

**Environmental implications of the study.** *Ab initio* calculations and DFMD simulations were performed to study  $^{90}\text{Sr}$  contamination and transmutation in C-S-H, the principal binding hydration product of cement.  $^{90}\text{Sr}$  and its daughter radionuclide  $^{90}\text{Y}$  were found to be stable in the cement paste, with a general preference for substituting Ca in the interlayer sites, where water enhances the possibilities for atomic bonding and charge transfer. This suggests that cement could be a good material to store the intermediate-half-life fission



product  $^{90}\text{Sr}$ , even in large concentrations. A mean field estimation gives a solubility limit of the order of 4% at room temperature, i.e., three  $^{90}\text{Sr}$  out of 72 Ca sites. It could be relevant in the context of nuclear waste storage under accidental conditions, for example in the Fukushima case where, to the best of our knowledge, a solution to the problem of storing the highly concentrated  $^{90}\text{Sr}$  after extraction from the emergency reactor cooling water has not been found yet.

The present work also showed that  $^{90}\text{Zr}$  (stable daughter nucleus of  $^{90}\text{Y}$ ) is not stable in Ca sites when the bulk phase of the corresponding elements at 0K is used as reference but stable when the hydrated form of the corresponding ions is used. The low substitution energies found for  $^{90}\text{Zr}$  in Si sites indicate that  $^{90}\text{Zr}$  could interfere with the silicate layers. Consequences of this result, such as possible modification of C-S-H mechanical properties by  $^{90}\text{Zr}$  migration or structural damage, should be further investigated and could benefit from the use of other simulation techniques such as classical force-field molecular dynamics simulations that can reach time scales of microseconds, as opposed to the picoseconds that can be achieved using DFMD.

## AUTHOR INFORMATION

### \*Corresponding Author

Andrés Saul

CINaM-CNRS UMR 7325

Campus de Luminy, 13288 Marseille Cedex 9, France

E-email: saul@cinam.univ-mrs.fr

## Notes

The authors declare no competing financial interest

## ACKNOWLEDGMENTS

The authors would like to acknowledge fruitful discussions with M. J. Abdolhosseini Qomi, K. J. Krakowiak, M. Bauchy, S. Yip, B. Coasne, H. Van Damme, and Mario del Popolo.

Part of this work was performed under the auspices of U. S. Department of Energy at Lawrence Livermore National Laboratory under contract DE-AC52-07A27344.

A. Caro work is supported by the Energy Dissipation to Defect Evolution Center (EDDE), an Energy Frontier Research Center funded by the U.S. Department of Energy, Office of Science.

---

<sup>1</sup> Weber, W. J.; Ewing, R. C.; Catlow, C. R. A.; de la Rubia Diaz, T. D.; Hobbs, L. W.; Kinoshita, C.; Matzke, H.; Motta, A. T.; Nastasi, M.; Salje, E. K. H.; Vancea, E. R.; Zinkle, S. J. Radiation effects in crystalline ceramics for the immobilization of high-level nuclear waste and plutonium. *J. Mater. Res.* **1998**, *13* (6), 1434-84.

<sup>2</sup> Ewing, R. C.; Weber, W. J.; Linard, F. W. Radiation effects in nuclear waste forms for high-level radioactive waste. *Prog. Nucl. Energ.* **1995**, *29* (2), 63-127.

<sup>3</sup> Wieland, R.; Bauer, T. H.; Morris, E. E. Status Report on Fast Reactor Recycle and Impact on Geologic Disposal. *Nucl. Technol.* **2007**, *154*.

<sup>4</sup> Kinoshita, N.; Sueki, K.; Sasa, K.; Kitagawa, J.-I.; Ikarashi, S.; Nishimura, T.; Wong, Y.-S.; Satou, Y.; Handa, K.; Takahashi, T.; Sato, M.; Yamagata, T. Assessment of individual radionuclide distributions from the Fukushima nuclear accident covering central-east Japan. *Proc. Natl. Acad. Sci.* **2011**, *108* (49), 19526-29.

<sup>5</sup> Chino, M.; Nakayama, H.; Nagai, H.; Terada, H.; Katata, G.; Yamazawa, H. Preliminary Estimation of Release Amounts of <sup>131</sup>I and <sup>137</sup>Cs Accidentally Discharged from the Fukushima Daiichi Nuclear Power Plant into the Atmosphere. *J. Nucl. Sci. Technol.* **2011**, *48* (7), 1129-34.

<sup>6</sup> Kobayashi, D.; Okouchi, T.; Yamagami, M.; Shinano, T. Verification of radiocesium decontamination from farmlands by plants in Fukushima. *J. Plant Res.* **2014**, *127* (1), 51-6.

<sup>7</sup> Shibata, T.; Solo-Gabriele, H.; Hata, T. Disaster Waste Characteristics and Radiation Distribution as a Result of the Great East Japan Earthquake. *Env. Sci. Tech.* **2012**, *46* (7), 3618-24.

<sup>8</sup> Atkins, M.; Glasser, F. Application of portland cement-based materials to radioactive waste immobilization. *Waste Manage.* **1992**, *12* (2-3), 105-31.

<sup>9</sup> Weber, W. Radiation effects in nuclear waste glasses. *Nucl. Instrum. Meth. B* **1988**, *32* (1-4), 471-9.

<sup>10</sup> Pascucci, M. R.; Hutchison, J. L.; Hobbs, L. W. The metamict transformation in alpha-quartz.

- 452 *Radiat. Eff.* **1983**, 74 (1-4), 219-26.
- 453 <sup>11</sup> Marks, N. A.; Carter, D. J.; Sassi, M.; Rohl, A. L.; Sickafus, K. E.; Uberuaga, B. P.;  
 454 Stanek, C. R. Chemical evolution via beta decay: a case study in strontium-90. *J. Phys.:  
 455 Condens. Matter* **2013**, 25 (6), 065504.
- 456 <sup>12</sup> Jiang, C.; Stanek, C.; Sickafus, K.; Uberuaga, B. First-principles prediction of disordering  
 457 tendencies in pyrochlore oxides. *Phys. Rev. B* **2009**, 79 (10), 104203.
- 458 <sup>13</sup> Jiang, C.; Uberuaga, B. P.; Sickafus, K. E.; Nortier, F. M.; Kitten, J. J.; Marks, N. A.;  
 459 Stanek, C. R. Using radioparagenesis to design robust nuclear waste forms. *Energy Environ.  
 460 Sci.* **2010**, 3 (1), 130-5.
- 461 <sup>14</sup> Mobasher, N.; Bernal, S. A.; Kinoshita, H.; Sharrad, C. A.; Provis, J. L. Gamma irradiation  
 462 resistance of an early age slag-blended cement matrix for nuclear waste encapsulation. *J. Mater.  
 463 Res.* **2015**, 30 (9), 1563-71.
- 464 <sup>15</sup> Jantzen, C.; Glasser, F.; Lachowski, E. Radioactive Waste-Portland Cement Systems: I, Ra-  
 465 dionuclide Distribution. *J. Am. Ceram. Soc.* **1984**, 67 (10), 668-73.
- 466 <sup>16</sup> Pareek, S.; Suzuki, Y.; Kimura, K.; Fujikura, Y.; Araki, Y. Radiation Shielding Properties and  
 467 Freeze-Thaw Durability of High-Density Concrete for Storage of Radioactive Contaminated Soil  
 468 in Fukushima. *Proceedings of the Int. Conference on Ageing of Materials and Structures* **2014**.
- 469 <sup>17</sup> Jantzen, C. M. Radioactive Waste-Portland Cement Systems: II, Leaching Characteristics. *J.  
 470 Am. Ceram. Soc.* **1984**, 67 (10), 674-6.
- 471 <sup>18</sup> Cau-dit Coumes, C. Alternative Binders to Ordinary Portland Cement for Radwaste Solidifica-  
 472 tion and Stabilization. In *Cement-Based Materials for Nuclear Waste Storage*; Bart, F.; Cau-di  
 473 Coumes, C.; Frizon, F.; Lorente, S., Eds.; Springer: New York, **2013** ; pp 171-191.
- 474 <sup>19</sup> Atkins, M.; Cowie, J.; Glasser, F.; Jappy, T.; Kindness, A.; Pointer, C. Assessment of the  
 475 Performance of Cement-Based Composite Material for Radioactive Waste Immobilization. *MRS  
 476 Proceedings* **1989**, 176, 117-27.
- 477 <sup>20</sup> Quilin, K.; Duerden, S.; Majumdar, A. Accelerated Ageing of Blended OPC Cements. *MRS  
 478 Proceedings* **1993**, 333, 341-8.
- 479 <sup>21</sup> Jiang, W.; Wu, X.; Roy, D. Alkali-Activated Fly Ash-Slag Cement Based Nuclear Waste Forms.  
 480 *MRS Proceedings* **1992**, 294, 255-60.
- 481 <sup>22</sup> Wieland, E.; Tits, J.; Kunz, D.; Dähn, R. Strontium Uptake by Cementitious Materials. *Env.  
 482 Sci. Tech.* **2008**, 42 (2), 403-9.

- 483 <sup>23</sup> Tits, J.; Wieland, E.; Muller, C.; Landesman, C.; Bradbury, M. Strontium binding by calcium  
484 silicate hydrates. *J. Colloid. Interf. Sci.* **2006**, *300* (1), 78-87.
- 485 <sup>24</sup> Evans, N. Binding mechanisms of radionuclides to cement. *Cem. Concr. Res.* **2008**, *38* (4),  
486 543-553.
- 487 <sup>25</sup> Youssef, M.; Pellenq, R. J.-M.; Yildiz, B. Docking <sup>90</sup>Sr radionuclide in cement: An atomistic  
488 modeling study. *Phys. Chem. Earth* **2014**, *70-71*, 39-44.
- 489 <sup>26</sup> Abdolhosseini Qomi, M.; Krakowiak, K.; Bauchy, M.; Stewart, K.; Shahsavari, R.; Jagan-  
490 nathan, D.; Brommer, D.; Baronnet, A.; Buehler, M.; Yip, S.; Ulm, F.-J.; Van Vliet, K.;  
491 Pellenq, R. J.-M. Combinatorial molecular optimization of cement hydrates. *Nat. Commun.*  
492 **2014**, *5*, 4960.
- 493 <sup>27</sup> Abdolhosseini Qomi, M.; Bauchy, M.; Ulm, F.-J.; Pellenq, R. J.-M. Anomalous composition-  
494 dependent dynamics of nanoconfined water in the interlayer of disordered calcium-silicates. *J.*  
495 *of Chem. Phys.* **2014**, *140* (5), 054515.
- 496 <sup>28</sup> Pellenq, R. J.-M.; Kushima, A.; Shahsavari, R.; Van Vliet, K. J.; Buehler, M. J.; Yip, S.;  
497 Ulm, F.-J. A realistic molecular model of cement hydrates. *Proc. Natl. Acad. Sci.* **2009**, *106*  
498 (38), 16102-7.
- 499 <sup>29</sup> Taylor, H. Nanostructure of CSH : Current status. *Advanced Cement Based Materials* **1993**, *1*  
500 (1), 38-46.
- 501 <sup>30</sup> Bonaccorsi, E.; Merlino, S.; Kampf, A. R. The Crystal Structure of Tobermorite 14 Å (Plom-  
502 bierite), a C-S-H Phase. *J. Am. Ceram. Soc.* **2005**, *88* (3), 505-12.
- 503 <sup>31</sup> Bonaccorsi, E.; Merlino, S.; Taylor, H. The crystal structure of jennite,  $\text{Ca}_9\text{Si}_6\text{O}_{18}(\text{OH})_6\text{H}_2\text{O}$ .  
504 *Cem. Concr. Res.* **2004**, *34* (9), 1481-8.
- 505 <sup>32</sup> Richardson, I. G. Tobermorite/jennite- and tobermorite/calcium hydroxide-based models for the  
506 structure of C-S-H: applicability to hardened pastes of tricalcium silicate,  $\beta$ -dicalcium silicate,  
507 Portland cement, and blends of Portland cement with blast-furnace slag, metakaolin, or silica  
508 fume. *Cem. Concr. Res.* **2004**, *34* (9), 1733-77.
- 509 <sup>33</sup> Richardson, I. G. The calcium silicate hydrates. *Cement and Concrete Research* **2008**, *38* (2),  
510 137-58.
- 511 <sup>34</sup> Allen, A. J.; Thomas, J. J.; Jennings, H. M. Composition and density of nanoscale calcium-  
512 silicate-hydrate in cement. *Nat. Mater.* **2007**, *6* (4), 311-6.
- 513 <sup>35</sup> Richardson, I. The nature of C-S-H in hardened cements. *Cem. Concr. Res.* **1999**, *29* (8),

1131-47.

- <sup>36</sup> Richardson, I. G.; Groves, G. W. Microstructure and microanalysis of hardened cement pastes involving ground granulated blast-furnace slag. *J. Mater. Sci.* **1992**, *27* (22), 6204-12.
- <sup>37</sup> Groves, G. W.; Le Sueur, P. J.; Sinclair, W. Transmission Electron Microscopy and Microanalytical Studies of Ion-Beam-Thinned Sections of Tricalcium Silicate Paste. *J. Am. Ceram. Soc.* **1986**, *69* (4), 353-6.
- <sup>38</sup> Kulik, D. A.. Improving the structural consistency of C-S-H solid solution thermodynamic models *Cement and Concrete Research* **2011**, *41*, 477–495.
- <sup>39</sup> Giannozzi, P. *et al.* QUANTUM ESPRESSO: a modular and open-source software project for quantum simulations of materials. *J. Phys.: Condens. Matter* **2009**, *21*, 395502.
- <sup>40</sup> Perdew, J. P.; Burke, K.; Ernzerhof, M. Generalized Gradient Approximation Made Simple. *Phys. Rev. Lett.* **1996**, *77* (18), 3865-8.
- <sup>41</sup> Tits, J.; Stumpf, T.; Rabung, T.; Wieland, E.; Fanghänel, T. Uptake of Cm(III) and Eu(III) by Calcium Silicate Hydrates: A Solution Chemistry and Time-Resolved Laser Fluorescence Spectroscopy Study. *Env. Sci. Tech.* **2003**, *37* (16), 3568-73.
- <sup>42</sup> Stumpf, T.; Tits, J.; Walther, C.; Wieland, E.; Fanghänel, T. Uptake of trivalent actinides (curium(III)) by hardened cement paste: a time-resolved laser fluorescence spectroscopy Study. *J. Colloid. Interf. Sci.* **2004**, *276*, 118-124.
- <sup>43</sup> Mandaliev, P.; Dähn, R.; Wehrli, B.; Wieland, E. Macro- and Microspectroscopic Study of Nd(III) Uptake Mechanisms in Hardened Cement Paste. *Env. Sci. Tech.* **2009**, *43* (21), 8462-8.
- <sup>44</sup> Mandaliev, P.; Dähn, R.; Tits, J.; Wehrli, B.; Wieland, E. EXAFS study of Nd(III) uptake by amorphous calcium silicate hydrates (C-S-H). *J. Colloid. Interf. Sci.* **2010**, *342* (1), 1-7
- <sup>45</sup> Marcus, Y. Thermodynamics of Solvation of ions. *J. Chem. Soc. Faraday Trans.* **1991**, *87* (18), 2995-9.
- <sup>46</sup> Messner, C. B.; Hofer T. S.; Randolph B. R.; Rode B. M. Structure and dynamics of the  $Zr^{4+}$  ion in water *Phys. Chem. Chem. Phys.* **2011**, *13*, 224-229.
- <sup>47</sup> Shannon, R. D.; Prewitt, C. T. Effective ionic radii in oxides and fluorides. *Acta Crystallogr. B* **1969**, *25* (5), 925-46.
- <sup>48</sup> Shannon, R. D. Revised effective ionic radii and systematic studies of interatomic distances in halides and chalcogenides. *Acta Crystallogr. A* **1976**, *32* (5), 751-67.
- <sup>49</sup> Gaona, X.; Dähn, R.; Tits, J.; Scheinost, A. C.; Wieland, E. Uptake of Np(IV) by CSH Phases

- 545 and Cement Paste: An EXAFS Study. *Env. Sci. Tech.* **2011**, *45* (20), 8765-71.
- 546 <sup>50</sup> Bonhoure, I.; Wieland, E.; Scheidegger, A. M.; Ochs, M.; Kunz, D. EXAFS Study of Sn(IV)  
547 Immobilization by Hardened Cement Paste and Calcium Silicate Hydrates. *Env. Sci. Tech.*  
548 **2003**, *37* (10), 2184-91.
- 549 <sup>51</sup> Bader, W. F. W. *Atoms in Molecules: A Quantum Theory*; Oxford University Press: New York,  
550 1990.
- 551 <sup>52</sup> Tang, W.; Sanville, E.; Henkelman, G. A grid-based Bader analysis algorithm without lattice  
552 bias. *J. Phys.: Condens. Matter* **2009**, *21* (8), 084204.

